VOL. 25, NO. 2, 2026, 90-98
elektrika.utm.my
EISSN 3083-9394

ELEKTRIKA
Journal of Electrical Engineering

The Effect of Windowing Function on the Accuracy Improvement of the High Directivity Millimeter Wave Antenna Characterization

Hana Arisesa[1,2], **Sevia Mahdaliza Idrus**[1*], **Farabi Iqbal**[1], **Yusuf Nur Wijayanto**[3], and **Purwoko Adhi**[2]

[1]Faculty of Electrical Engineering, Universiti Teknologi Malaysia, 81310 UTM Skudai, Johor, Malaysia.
[2]Research Centre for Telecommunication, National Research and Innovation Agency, BRIN Bandung Indonesia.
[3]Research Centre for Electronics, National Research and Innovation Agency, BRIN Bandung Indonesia.

[*]Corresponding author: sevia@utm.my

Abstract: High-gain antennas can be used to compensate for attenuation in millimeter-wave communication technology. So, the antenna's characterization is vital for both the measurement results' accuracy and the measurement setup. High-gain reflector antennas can be characterized using the near-field method, where the antenna's radiation measurement is conducted in the near-field region and then transformed into far-field values using Fourier transformation with the Fast Fourier Transform algorithm. To achieve better accuracy, this technique requires the application of several methods. This paper discusses how the selection of window functions, which are applied before the Fourier transform, influences the production of antenna characteristics with high accuracy by reducing spectral leakage from the data. Ten window functions commonly used in data processing will be tested for their accuracy in antenna parameters such as 3-dB and 10-dB bandwidth, as well as antenna null parameters around the main lobe. Two window functions that can be used in applications related to this research are the Gaussian window and the Tukey window, providing more detailed antenna characteristics.

Keywords: High-gain, Windowing Function, mm-wave, Near-field measurement

Article History: received 21 June 2025; accepted 12 June 2026; published 31 August 2026
Digital Object Identifier 10.11113/elektrika.v25n2.760

1. INTRODUCTION

Millimeter wave communication is becoming one of the future wireless communication technologies expected to deliver 5G and beyond communication technology. This technology is capable of providing services and applications that differ from current wireless technologies in terms of speed, security, reliability, and latency. The current millimeter frequency band offers more bandwidth, enabling these advantages [1, 2].

Nevertheless, wireless communication technology using the millimeter frequency band has other challenges, such as extreme propagation issues. Atmospheric attenuation, such as phenomena like rain, fog, dust, snow, diffraction, and interference, causes signal loss in the link [3]. The attenuation increases as the frequency increases, leading to challenging signal compensation in the higher frequency. In wireless communication, signal strength is crucial to providing excellent communication quality.

One technique to compensate for the significant attenuation loss at millimeter wave frequencies involves using high-gain antennas on both the transmitter and receiver sides. The use of high-gain antennas for 5G communication links has become one of the demonstrated solutions. The use of high-gain antennas is capable of providing sufficient compensation for the implementation of wireless communication, such as backhaul links [4]. Moreover, with the increasing frequency, the physical dimensions of the antenna become smaller and more suitable for use in real-world environments.

The problem that arises in the use of high-gain antennas is how to characterize the antenna. The standard for antenna measurement uses an anechoic chamber for an antenna characterization process that requires the use of an outdoor test site (over the air, OTA) and time-consuming measurements. Furthermore, obtaining more accurate measurements requires a wider area beyond the far-field antenna region. Unfortunately, anechoic chambers generally cannot accommodate the far-field area required by high-gain antennas. Therefore, researchers have developed near-field antenna measurements, which do not require a large measurement area [5, 6].

Large anechoic chambers or far-field distances are not necessary for the precise characterization of an antenna's radiation pattern, gain, and directivity thanks to the widely used near-field (NF) to far-field (FF) transformation technique. The far-field radiation parameters can be accurately estimated by sampling the electromagnetic fields in the near-field region of the antenna, which is usually over a planar, cylindrical, or spherical surface, and then using mathematical transformations like Fourier analysis or modal expansion [7, 8].

Large antennas or applications where space restrictions preclude direct far-field measurements benefit greatly from this technique. Spiral scanning patterns [9], linear phase retrieval for phase less measurements [10], and surface-source-based transformations that enhance conditioning and precision are some recent developments that have increased the speed, accuracy, and robustness of NF–FF techniques [11]. Additionally, NF–FF algorithms have been optimized to handle irregular and incomplete measurement data [12] and customized for use with robotic scanning systems in industrial settings [13]. These developments keep improving the NF-FF transformations' suitability and dependability in contemporary antenna testing settings.

Antenna measurements that utilize near-field techniques will convert near-field antenna measurement data into far-field antenna measurement data through a near-field to far-field transformation. This transformation mainly focuses on the use of the fast Fourier transform (FFT) to obtain the desired antenna characterization results. The transformation process requires other techniques, such as phase correction [14], windowing function [15], and probe correction [16], to achieve antenna characterization results.

In this article, the effects of selecting a windowing function on the accuracy of measurement results and high-gain antenna estimation will be explained. Ten well-known window functions are used to analyze near-field antenna measurement data so that the accuracy level of far-field antenna characteristics for each window function can be determined. The detailed comparison of each window for main lobe information will be discussed. The suggestion on the best window function will be examined based on the data analysis.

2. HIGH DIRECTIVITY ANTENNA CHARACTERIZATION

2.1 Antenna Parameters

A high directivity antenna is an antenna that concentrates its radiation or reception in a particular direction, rather than dispersing it uniformly in all directions like an omnidirectional antenna. Additionally, the antenna's ability to direct the signal results in a high gain. The directivity and gain of the antenna have a proportional relationship, which can be described by

$$G = \eta \times D \tag{1}$$

Gain (G) and directivity (D) are dimensionless, as η is the efficiency of the antenna.

This high-directivity antenna can be realized using a parabolic dish antenna or a Yagi-Uda antenna, which can focus the signal into a particular direction. In the millimeter wave communication link, high directivity can be utilized to reduce the atmospheric attenuation loss. These advantages can be applied to point-to-point communication links, long-distance communication, or specific targeting direction. The approximate parabolic dish antenna gain can be calculated as follows [17]:

$$Gain\ (G) = \eta \left(\frac{\pi D}{\lambda}\right)^2 \tag{2}$$

where η is antenna efficiency, and D is antenna dish diameter. Other antenna parameters that are useful to describe an antenna are 3 dB antenna bandwidth, radiation pattern, bandwidth, and side lobe level (SLL).

The basic method for antenna measurement requires a specific test area. In order to obtain accurate measurement result, the antenna under test must be satisfy formula as follows:

$$R \geq \frac{2D^2}{\lambda} \tag{3}$$

where R is the minimum distance to be considered "far-field," D is the largest dimension of the antenna aperture (meters), and λ is the wavelength (meters).

2.2 Windowing Function

The NF to FF method for antenna measurements necessitates the conversion of NF measurement data into FF data through the Fourier Transform. To achieve optimal antenna characterization results, the measurement data must be windowed to reduce side lobes and spectral leakage before performing the Fourier Transform using the Fast Fourier Transform (FFT) algorithm.

Windowing is the process of multiplying your data with a smooth tapering function. Several window functions are available for use in signal analysis. This section briefly describes several window functions that will be used in processing antenna measurement data. Each windowing function will be displayed with the equation that describes the window function, along with its representation in the time domain and its frequency response. For this purpose, 64 data samples were used, and the FFT size is 2084 points.

2.2.1 Bartlett Window

Bartlett window can be described using equation

$$w(n) = \frac{2}{M-1}\left(\frac{M-1}{2} - \left|n - \frac{M-1}{2}\right|\right) \tag{4}$$

The Bartlett window is also known as the Fejer or Triangle window.

Figure 1 describes the Bartlett window in the time domain representation (above) and its frequency response. The window analytically can be represented by Equation (4). It can be inferred that the Bartlett window has a side lobe level of -25 dB. The variable *n* is the number of samples in the measurement. For the purpose of illustrating the window function, in this case, *n* is chosen to be 64 samples. However, in the analysis, the value of n will be adjusted based on the number of samples collected during the actual measurement.

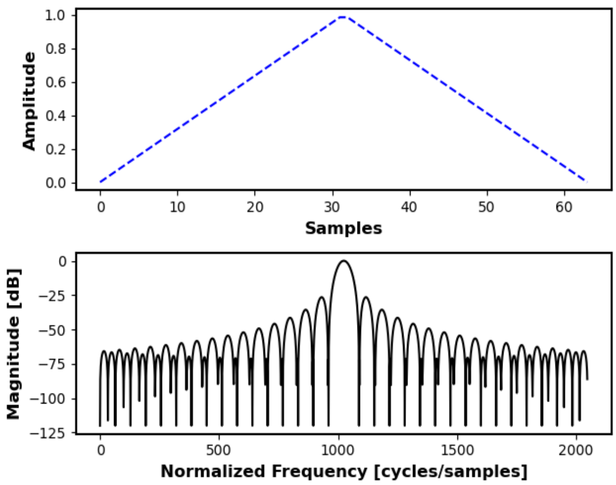

Figure 1. Bartlett window with 64 samples (above) and its frequency response (below).

2.2.2 Gaussian Window

The Gaussian window can be described using an equation as follows:

$$w(n) = e^{-0.5\left(\frac{n}{a}\right)^2} \tag{5}$$

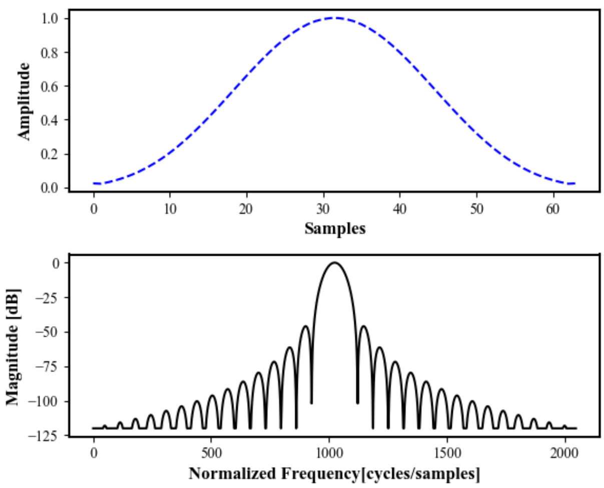

Figure 2. Gaussian window function with 64 samples (above) and its frequency response (below).

Figure 2 shows the Gaussian window function representation in the time domain (above) and its frequency response (below), which σ is 7. The Gaussian window function can be represented by Equation (5), where sigma (σ) is the standard deviation. The Gaussian window is suitable for good time-frequency localization.

2.2.3 Dolph-Chebyshev Window

The frequency response describes the Dolph-Chebyshev window function as follows:

$$W(k) = \frac{cos\{Mcos^{-1}\left[\beta\ cos\left(\frac{\pi k}{M}\right)\right]\}}{cosh[M\ cosh^{-1}(\beta)]} \tag{6}$$

where

$$\beta = cosh\left[\frac{1}{M} cosh^{-1}\left(10^{\frac{A}{20}}\right)\right]$$

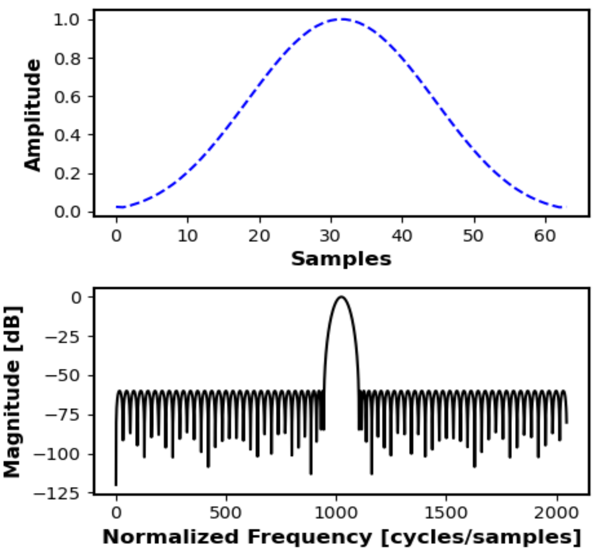

Figure 3. Dolph-Chebyshev window function (above) for 64 samples and its frequency response (below).

Figure 3 shows Dolph-Chebyshev window function in the time domain (above) and its frequency response (below). The window function can be approached by Equation (6). The window function has advantages in maximum control over sidelobe height. The desired sidelobe level in decibels can be determined by attenuation values (A). It is depicted that the attenuation level was set to 60 dB, so the side lobe level is flat at -60 dB.

2.2.4 Hann Window

Hann window can be described using formula

$$w(n) = 0.5 - 0.5\ cos\left(\frac{2\pi n}{M-1}\right)\quad 0 \le n \le M-1 \tag{7}$$

which $w(n)$ is the Hann window function. M is the number of points in the output window.

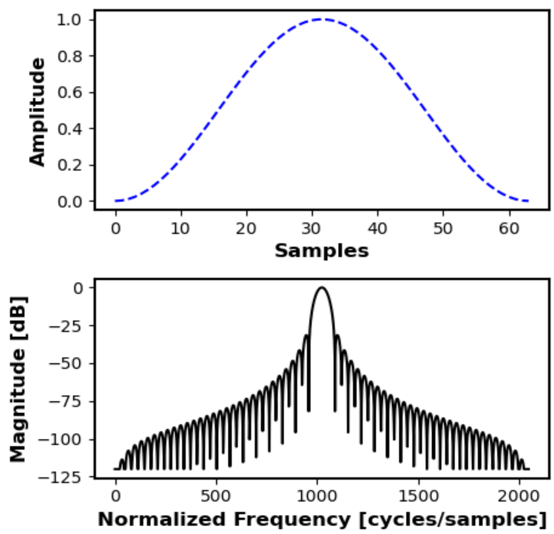

Figure 4. Hann window function with 64 samples (above) and its frequency response (below).

Figure 4 depicted the Hann window function of 64 samples in the time domain (above) and its frequency response (below). The Hann window uses a tapered window function to reduce spectral leakage by smoothly bringing the signal to zero at the edges. The Hann window is defined as Equation (7). It has around -31 dB for the first side lobe.

2.2.5 Hamming Window

Hamming window can be described using formula

$$w(n) = 0.54 - 0.46\,cos\left(\frac{2\pi n}{M-1}\right)\; 0 \leq n \leq M-1 \quad (8)$$

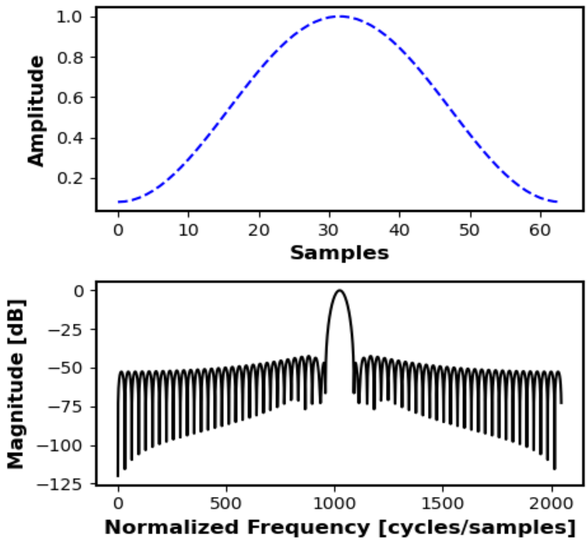

Figure 5. Hamming window function with 64 samples (above) and its frequency response (below)

Figure 5 depicted the Hamming window function of 64 samples in the time domain (above) and its frequency response (below). The Hamming window uses a tapered window function similar to the Hann Window. However, the Hamming window provides improved suppression of side lobes. The Hamming window has -41 dB for the first side lobe, compared to the Hann window's -31 dB. The Hamming window is defined as Equation (8).

2.2.6 Blackman Window

Blackman window can be described using formula

$$w(n) = 0.42 - 0.5\,cos\left(\left(\frac{2\pi n}{M}\right) + 0.08\,cos\left(\frac{4\pi n}{M}\right) \quad (9)$$

Figure 6 shows the Blackman window function (above) and its frequency response (below), both based on 64 samples of data. The Blackman window has a smooth, bell-like shape with zero values (or near zero) at the edges. It performs better in reducing spectral leakage, achieving a side lobe attenuation of approximately 59 dB. However, the Blackman window introduces a wider main lobe compared to the Hamming window. The window is defined as Equation (9).

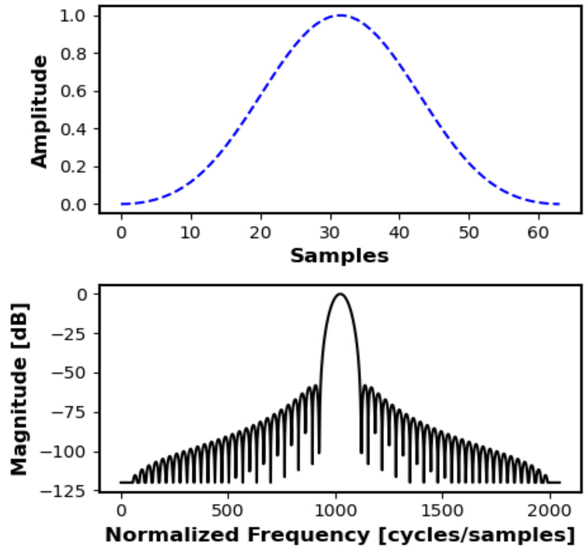

Figure 6. Blackman window function with 64 samples (above) and its frequency response (below)

2.3.7 Tukey Window

Tukey window often called cosine-tapered windows. It can be described using the following formula:

$$w(n) = 1.0 \text{ for } 0 \leq |n| \leq \alpha\frac{M}{2} \quad (10)$$

$$w(n) = 0.5\left[1.0 + cos\left[\pi\frac{n - \alpha\frac{M}{2}}{2(1-\alpha)\frac{M}{2}}\right]\right]$$

$$\text{for } \alpha\frac{M}{2} \leq |n| \leq \frac{M}{2}$$

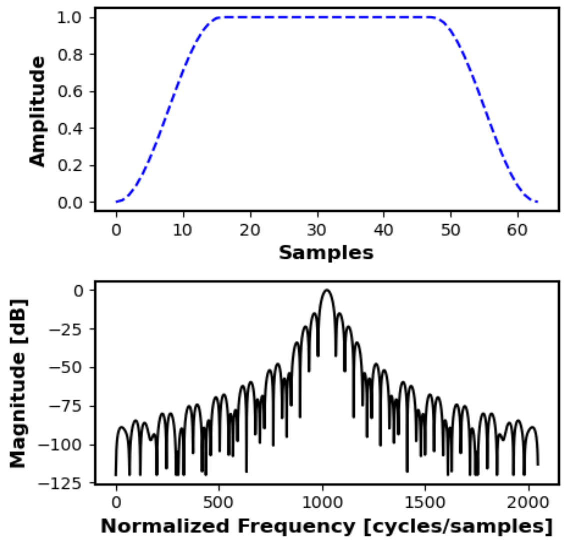

Figure 7. Tukey window function with 64 samples (above) and its frequency response (below).

Figure 7 shows the Tukey window function (above) and its frequency response (below), both based on 64 samples of data, for $\alpha = 0.5$. The Tukey uses a tapered cosine window. It has control over the tapering ratio (α) as shown in Equation (10). The Tukey window offers a smooth transition between a rectangular window and a Hann window.

2.3.8 Kaiser Window

Kaiser window can be described using formula

$$w(n) = I_0\left(\beta\sqrt{1-\frac{4n^2}{(M-1)^2}}\right) / I_0\beta \tag{11}$$

$$\text{with } -\frac{M-1}{2} \leq n \leq \frac{M-1}{2}$$

Figure 8 is the Kaiser window function (above) and its frequency response (below), whose formula can be described by Eq. 11, which I_0 is the modified zeroth-order Bessel function. It allows control over the side lobe level (SLL) and main lobe width through a parameter β. The Kaiser window correlates with other window functions. If $\beta = 5$, then it is similar to the Hamming window; if $\beta = 6$, it similar to the Hann window; if $\beta = 8.6$ then it is similar to the Blackman window.

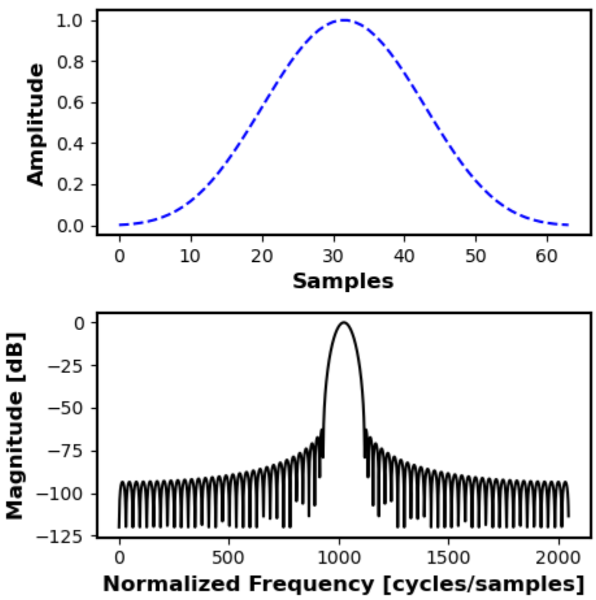

Figure 8. Kaiser window function with 64 samples (above) and its frequency response (below)

2.3.9 Parzen Window

Parzen window can be described using formula

$$w(n) = 1.0 - 6\left[\frac{n}{N/2}\right]^2\left[1.0-\frac{|n|}{N/2}\right] \; 0 \leq |n| \leq \frac{N}{4}$$

$$w(n) = 2\left|1.0-\frac{|n|}{N/2}\right|^3 \text{ for } \frac{N}{4} \leq |n| \leq \frac{N}{2} \tag{12}$$

Figure 9 shows the Parzen window function (above) and its frequency response (below) for 64 samples of data. The Parzen window is a tapering function characterized by a smooth, bell-shaped profile, similar to Gaussian, Hamming, Hanning, or Blackman windows. The function has zero value at the edge, offering a reduction of the spectral leakage. It has a low side lobe level of -50 dB with a moderate mainlobe width. The window can be represented analytically by Equation (12).

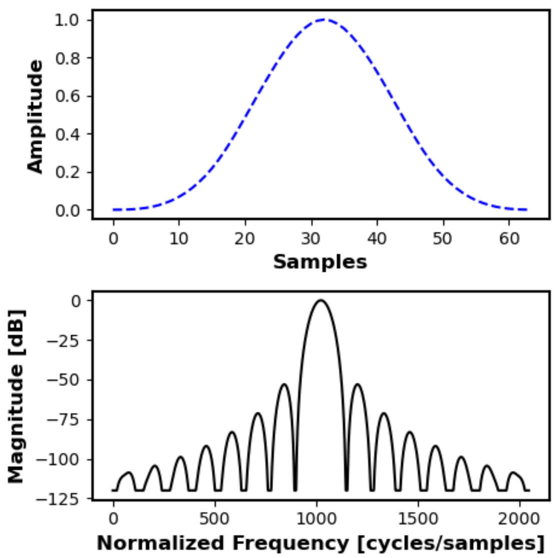

Figure 9. Parzen window function with 64 samples (above) and its frequency response (below)

2.3.10 Bohman Window

Bohman Window can be described using equation

$$w(n) = \left[1.0-\frac{|n|}{M/2}\right] cos\left[\pi\frac{|n|}{M/2}\right] + \frac{1}{\pi} sin\left[\pi\frac{|n|}{M/2}\right] \tag{13}$$

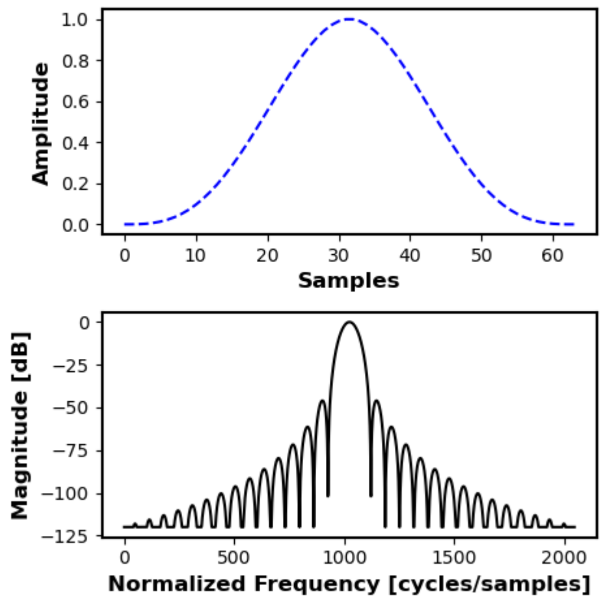

Figure 10. Bohman window function with 64 samples (above) and its frequency response (below).

Figure 10 depicted the Bohman window function of 64 samples in the time domain (above) and its frequency response (below). The Bohman window offers zero value at the edges. The Bohman window is analytically defined as Equation (13). It has a side lobe level of -31 dB for the first side lobe. As depicted in the frequency response, the window has sidelobe decay quickly, which helps suppress leakage from nearby frequencies.

3. ANTENNA MEASUREMENT

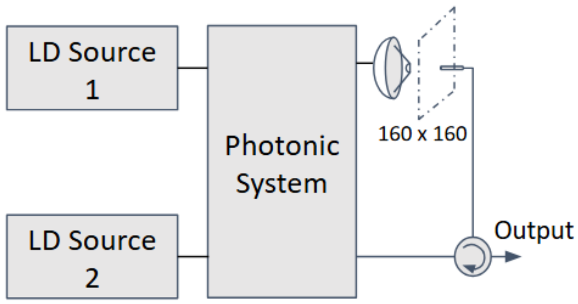

Figure 11. The measurement setup

Figure 11 shows the antenna measurement setup. The high directional Cassegrain antenna has been characterized based on the photonic system in a near-field region [6]. The Cassegrain antenna has a main reflector diameter of 152 mm and operates at a 300 GHz frequency. The antenna has a sub-reflector in the center front of the antenna supported by four rods. In the near-field region of the antenna, the measurement system scanned the two-dimensional (2D) distribution amplitude and phase of the antenna in the area of 160 x 160 mm with 0.25 mm resolution. The electromagnetic (EM) wave sensor is positioned 5 cm in front of the antenna to capture the antenna's EM radiation. The motorized linear scanning captured the EM wave point by point, producing data with a resolution of 0.25 mm, resulting in 640 samples along the X and Y axes.

4. RESULTS AND DISCUSSION

Figures 12 and 13 show the 2D amplitude and phase distribution of the antenna measurement. In the 2D amplitude profile, artifacts of the support rods are clearly seen in the measurement results. The four support beams of the sub-reflector obstruct the antenna's signal emission, which creates shadow artifacts on both the vertical and horizontal diagonals. At the center of the antenna, the influence of the sub-reflector, which also obstructs the antenna signal, is also visible. The maximum amplitude of the signal occurs at the center of the antenna, which then decreases toward the edge of the antenna disk.

The two-dimensional phase distribution measurement results show that the measured phase matches the predicted phase. The phase distribution does not fluctuate significantly, despite shadow artifacts caused by the support rod and sub-reflector that are clearly seen in the profile. However, some outer parts of the measurement results experience sharp phase fluctuations due to noise from the measurement system. The radiation phase of the antenna signal mapped to the profile produces characteristic circles corresponding to the diameter of the main reflector antenna. Outside the main reflector antenna, the obtained signal is noise, as seen in Figures 12 and 13.

To obtain the characterization of the antenna's radiation pattern, the near-field measurement data in the form of 2D amplitude and phase distribution needs to be transformed into far-field antenna data using Fourier transformation. To reduce spectral leakage in this transformation, windowing is necessary. The effects of ten types of windowing functions commonly used for data analysis will be explained.

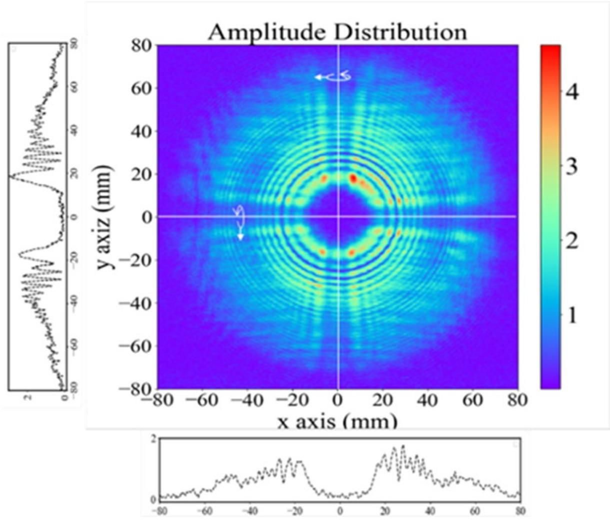

Figure 12. The 2D amplitude distribution of the antenna measurement.

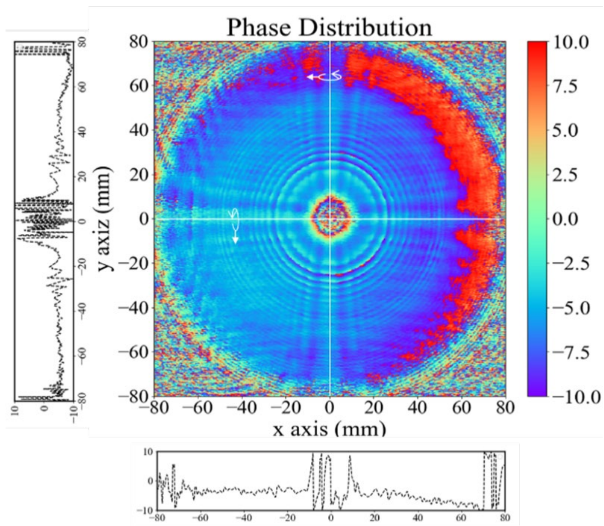

(b)

Figure 13. The 2D phase distribution of the antenna measurement.

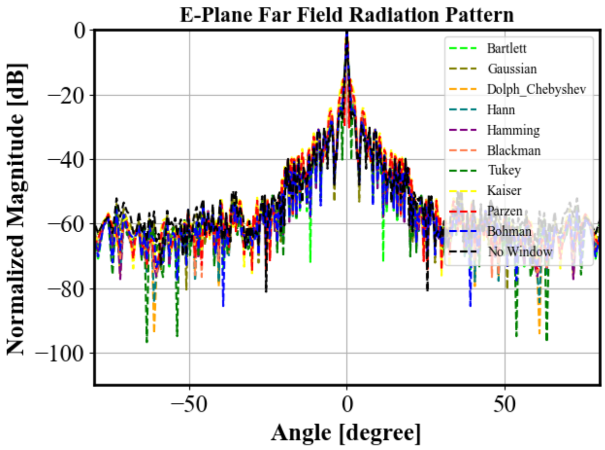

Figure 14. The E-Field antenna radiation pattern due to window function varieties.

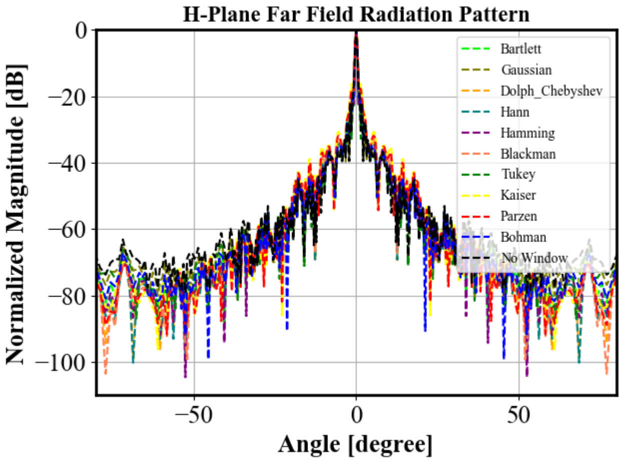

Figure 15. The H-Field antenna radiation pattern due to window function varieties.

Figures 14 and 15 illustrate the antenna radiation pattern for the E-plane and H-plane with variations in the windowing function. The antenna radiation has a sharp main lobe (pencil beam) characteristic in both the E-plane and H-plane radiation. The E-plane and H-plane antenna radiation without using a windowing function are almost identical, with a cross-correlation of 0.8. Because this antenna is one that has high directivity, most of the energy will be radiated. The antenna gain is calculated to be 49.6 dBi using Equation (2), assuming the standard reflector antenna efficiency of 0.4.

We will discuss the impact of the windowing function on reducing spectral leakage in the main lobe, given the significance of this information. Figure 16 provides detailed information about the antenna radiation pattern for the E-plane around the main lobe at an angle of ±2 degrees, highlighting the differences in data processing due to various windowing functions. Each window function has a different effect on the results of the antenna radiation pattern. The 3-dB and 10-dB beamwidth and radiation null will be discussed. The null is defined by a value that is lower than both its right and left sides. The zero degree is the center of the main lobe. In general, the several window functions have different effects compared to each other.

Measuring the 3-dB bandwidth of the main lobe for each window function is useful to describe the antenna main lobe characteristics. Without a windowing function, the 3-dB bandwidth antenna is 0.22°. However, when the window function is introduced, the 3-dB bandwidth becomes wider. There are only two window functions that are similar to without windowing: Gaussian window and Tukey window, which are 0.26°. The other windows have an effect on widening the 3-dB bandwidth, especially the Blackman, Kaiser, and Parzen windows, more than twice compared to without windowing, which are 0.44°, 0.6°, and 0.5°, respectively.

For the 10-dB bandwidth, using no windowing is the best option for analyzing antenna measurement data. Without windowing, the bandwidth is 0.76°. Other windows give the bandwidth more than 0.8°. The closed window function results only Gaussian, Blackman, and Parzen, which are 0.88°.

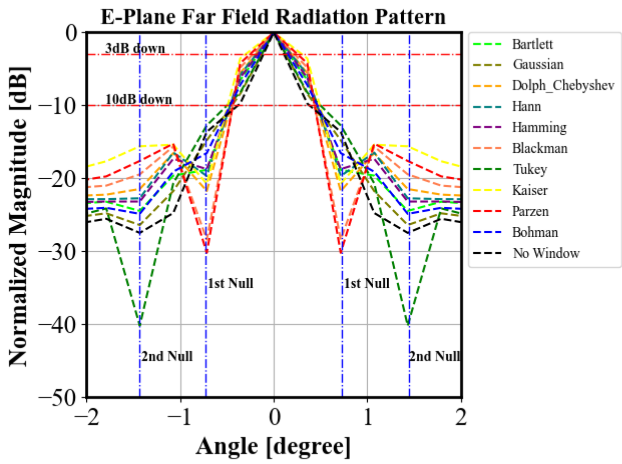

Figure 16. The E-Field antenna radiation pattern due to window function varieties.

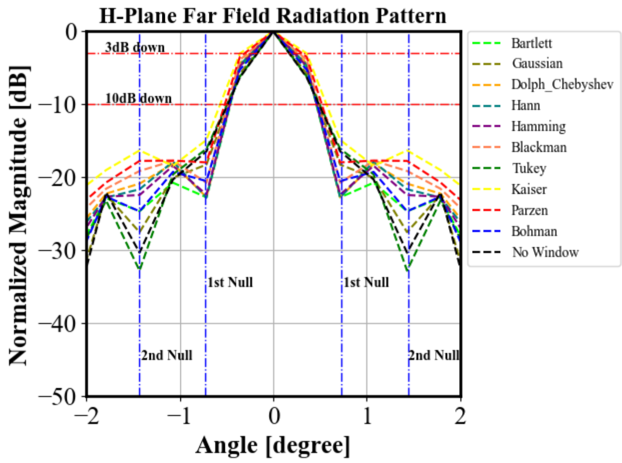

Figure 17. The antenna radiation pattern H-Field due to window function varieties.

All scenarios, with and without the windowing function, do not exhibit a second null for ±0.2°. However, the Tukey window is the most effective window function, achieving the lowest first null at -40.18 dB, while the Parzen and Blackman windows follow with first nulls of -

30.19 dB and -28.39 dB, respectively for the second and the third.

Figure 17 shows the detailed information about the antenna radiation pattern for the H-plane around the main lobe at an angle of ±2 degrees. Generally, there are no characteristic differences from the E-plane result, but in detail, there are some significant differences. While there aren't any notable distinctions from the E-plane in general, there are some noteworthy ones in particular. For the 3-dB bandwidth, the value is larger than that of the E-plane, with no window and the Tukey window producing the smallest 3-dB bandwidth of 0.34 degrees, followed by the Gaussian window at 0.36 degrees. The widest bandwidth is achieved using the Kaiser window at 0.7 degrees. For the 10-dB Bandwidth, it is generally larger than the E-Plane, with the Bartlett, Gaussian, Dolby-Chebyshev, Hann, and Hamming windows resulting in the narrowest 10-dB bandwidth of 0.92 degrees. Blackman, Tukey, and without a window will produce a bandwidth of 0.98 degrees. Meanwhile, Kaiser and Parzen window functions produce a 10-dB bandwidth greater than 1 degree.

For the H-plane, there is a significant difference in producing null details around the main lobe compared to the E-plane. Some window functions can reveal the first and second nulls in the antenna radiation pattern over a span of two degrees. Bartlett and Bohman windows fall into this category. In contrast, the rectangular window and Tukey window exhibit nearly identical characteristics. However, the Tukey window is better at displaying the 2nd null at -32.79 dB compared to no window at around -30.32 dB. Table 1 and Table 2 show the complete details of the antenna parameters for the 3-dB bandwidth, 10-dB bandwidth, and first and second null of each scenario.

Table 1. The E-Field antenna radiation pattern

Window Function	3 dB BW (°)	10 dB BW (°)	1st Null (dB)	2nd Null (dB)
No Window	±0.11	±0.38	-27.52	**NA**
Bartlett	±0.16	±0.46	-24.47	**NA**
Gaussian	±0.13	±0.44	-26.41	**NA**
DC	±0.19	±0.45	-21.75	**NA**
Hann	±0.18	±0.46	-19.68	**NA**
Hamming	±0.17	±0.46	-18.74	**NA**
Blackman	±0.22	±0.44	-28.39	**NA**
Tukey	±0.13	±0.49	-40.18	**NA**
Kaiser	±0.30	±0.49	-20.75	**NA**
Parzen	±0.25	±0.44	-30.19	**NA**
Bohman	±0.16	±0.46	-24.87	**NA**

Table 2. The H-Field antenna radiation pattern

Window Function	3 dB BW (°)	10 dB BW (°)	1st Null (dB)	2nd Null (dB)
No Window	±0.17	±0.49	**NA**	-30.32
Bartlett	±0.22	±0.46	-22.74	-24.64
Gaussian	±0.18	±0.48	**NA**	-27.52
DC	±0.24	±0.46	-22.72	**NA**
Hann	±0.24	±0.46	-22.78	**NA**
Hamming	±0.22	±0.46	-22.36	**NA**
Blackman	±0.27	±0.49	-20.74	**NA**
Tukey	±0.17	±0.49	**NA**	-32.79
Kaiser	±0.35	±0.57	-18.44	**NA**
Parzen	±0.31	±0.53	-17.89	**NA**
Bohman	±0.21	±0.47	-20.54	-24.67

3. CONCLUSION

The analysis of using window functions for accurate measurement of high-gain antenna characteristics has been conducted. From the discussion results, it can be concluded that the Gaussian and Tukey windows can be used to provide better detail of antenna characteristics compared to other window functions. Having clear and detailed information about antenna characteristics, especially for high directional antennas, is important for practical uses, particularly for point-to-point wireless communication, because these antennas focus their main signal in a specific direction with a very narrow angle. The results of this research can be applied to provide an illustration of the appropriate selection of window functions in this application.

ACKNOWLEDGMENT

The authors would like to thank Universiti Teknologi Malaysia and BRIN Bandung, Indonesia, for their support in conducting this research.

REFERENCES

[1] Y. Niu, Y. Li, D. Jin, L. Su, and A. V. Vasilakos, "A survey of millimeter wave communications (mmWave) for 5G: opportunities and challenges," *Wireless Networks*, vol. 21, no. 8, pp. 2657–2676, Apr. 2015, doi: https://doi.org/10.1007/s11276-015-0942-z.

[2] T. S. Rappaport and E. Al, *Millimeter wave wireless communications*. New Jersey: Prentice Hall, 2015.

[3] A. A. Budalal *et al.*, "Millimetre-Wave Propagation Channel Based on NYUSIM Channel Model With Consideration of Rain Fade in Tropical Climates," *IEEE Access*, vol. 10, pp. 1990–2005, 2022, doi: https://doi.org/10.1109/access.2021.3135382.

[4] T. Kürner *et al.*, "THz Communications and the Demonstration in the ThoR–Backhaul Link," *IEEE Transactions on Terahertz Science and Technology*, vol. 14, no. 5, pp. 554–567, Jun. 2024, doi: https://doi.org/10.1109/tthz.2024.3415480.

[5] R. C. Johnson, H. A. Ecker, and J. S. Hollis, "Determination of far-field antenna patterns from near-field measurements," *Proceedings of the IEEE*, vol. 61, no. 12, pp. 1668–1694, 1973, doi: https://doi.org/10.1109/proc.1973.9358.

[6] J. Lai and Y. Yang, "3D Terahertz Antenna Measurement: A comparison between solid-state electronics and photomixing approaches," *IEEE*

Antennas and Propagation Magazine, vol. 66, no. 4, pp. 37–50, Jun. 2024, doi: https://doi.org/10.1109/map.2024.3405312.

[7] H. Arisesa, Yusuf Nur Wijayanto, Purwoko Adhi, F. Iqbal, and S. M. Idrus, "Fast prediction of a high directivity antenna characterization for future wireless communication based on terahertz photonics," *Journal of Physics Conference Series*, vol. 2696, no. 1, pp. 012012–012012, Jan. 2024, doi: https://doi.org/10.1088/1742-6596/2696/1/012012.

[8] Y. Tanaka *et al.*, "Photonics-Based Near-Field Measurement and Far-Field Characterization for 300-GHz Band Antenna Testing," *IEEE Open Journal of Antennas and Propagation*, vol. 3, pp. 24–31, Dec. 2021, doi: https://doi.org/10.1109/ojap.2021.3133470.

[9] R. Cicchetti, F. D'Agostino, F. Ferrara, C. Gennarelli, R. Guerriero, and M. Migliozzi, "Near-Field to Far-Field Transformation Techniques with Spiral Scannings: A Comprehensive Review," *International Journal of Antennas and Propagation*, vol. 2014, pp. 1–13, 2014, doi: https://doi.org/10.1155/2014/143084.

[10] A. Paulus, J. Kornprobst, J. Knapp, and T. F. Eibert, "Linear Phase Retrieval for Near-Field Measurements with Locally Known Phase Relations," *2022 16th European Conference on Antennas and Propagation (EuCAP)*, vol. 17, pp. 1–5, Mar. 2021, doi: https://doi.org/10.23919/eucap51087.2021.9411328.

[11] J. Kornprobst, J. Knapp, R. A. M. Mauermayer, O. Neitz, A. Paulus, and T. F. Eibert, "Accuracy and Conditioning of Surface-Source Based Near-Field to Far-Field Transformations," *IEEE Transactions on Antennas and Propagation*, vol. 69, no. 8, pp. 4894–4908, Aug. 2021, doi: https://doi.org/10.1109/tap.2020.3048497.

[12] G. Schnattinger, C. Lopez, E. Kılıç, and T. F. Eibert, "Fast near-field far-field transformation for phaseless and irregular antenna measurement data," *Advances in radio science*, vol. 12, pp. 171–177, Nov. 2014, doi: https://doi.org/10.5194/ars-12-171-2014.

[13] S. F. Gregson and C. G. Parini, "A Comparison of Near-Field to Far-Field Transformation Techniques For Use With Industrial Multi-Axis Robotic Antenna Measurement Systems," *2022 16th European Conference on Antennas and Propagation (EuCAP)*, pp. 1–5, Mar. 2024, doi: https://doi.org/10.23919/eucap60739.2024.10501489.

[14] N. V. Anyutin, I. M. Malai, M. A. Ozerov, A. V. Titarenko, and M. S. Shkurkin, "Correction of the Measured Amplitude-Phase Field Distribution in the Near Field from the Directional Pattern of the Probe," *Measurement Techniques*, vol. 61, no. 1, pp. 67–71, Apr. 2018, doi: https://doi.org/10.1007/s11018-018-1389-2.

[15] Sulistyaningsih, et al. "Performance Comparison of Blackman, Bartlett, Hanning, and Kaiser Window for Radar Digital Signal Processing". in *2019 4th International Conference on Information Technology, Information Systems and Electrical Engineering (ICITISEE)*. 2019.

[16] M.M. Leibfritz and P.M. Landstorfer, "Full probe-correction for near-field antenna measurements," *2006 IEEE Antennas and Propagation Society International Symposium*, pp. 437–440, Jan. 2006, doi: https://doi.org/10.1109/aps.2006.1710552.

[17] C. A. Balanis, *Antenna Theory Analysis and Design*, 4th ed. Hoboken, New Jersey Wiley, 2016.